Autonomous FSM Architecture for Commissioning and Differential Drag Control in CubeSat Formations

Elías Obreque-Sepúlveda, Robert T. Wicks, Nassima Khorchef, Eamon Scullion,
Amna Riaz, Richard Binns, and Jethro Vernon
Dept. of Mathematics, Physics and Electrical Engineering
Northumbria University
Newcastle upon Tyne, UK

***Abstract*—The operational success of inter-satellite laser link (ISL) missions in CubeSat constellations depends on the strict management of conflicting requirements: energy harvesting, high-precision payload targeting, and orbital maintenance. This paper presents an automated onboard mission logic designed to manage the relative distance of a two-satellite 6U in formation flight (ranging from 100 km to 1000 km) using differential drag as the sole propellantless maneuvering mechanism.**

The main contribution is a deterministic decision-making framework based on a finite-state machine (FSM) that governs transitions between operational modes of the ADCS. These modes, including maximum and minimum drag, ground station tracking, and high-precision laser pointing, are prioritized to modulate the ballistic coefficient between minimum and maximum drag while respecting mission constraints. To ensure mission feasibility, the logic incorporates experimentally derived power and consumption profiles from laboratory characterization of satellite subsystems, while maintaining confidentiality regarding specific hardware components.

The proposed logic is validated using Basilisk, an open-source high-fidelity simulator, incorporating gravitational perturbations and a facet-based aerodynamic model. The results on the first stage of the orbit simulation demonstrate that this drag-based differential logic can achieve a relative drift greater than 400 km per month while maintaining energy balance for operation. In addition, it allows quantification of approximate ballistic coefficients in early stages. Finally, we discuss the potential of parallel learning algorithms to augment the FSM, identifying environmental clusters and predicting energy trends to further optimize deterministic transitions under realistic operational constraints.

***Index Terms*—differential drag, formation flying, finite state machine, CubeSat, ADCS mode management, power budget, autonomous commissioning**

I. Introduction

Differential drag has established itself as a viable propellantless formation control technique for low-Earth-orbit constellations, from early theoretical formulations [1], [2] to operational deployment at scale [3], [4]. By modulating the cross-sectional area presented to the atmospheric flow, a net differential deceleration is created between spacecraft, producing a controllable secular drift without propellant expenditure. For CubeSat platforms, where volume, mass, and power preclude conventional thrusters, differential drag is often the only viable means of orbit-relative manoeuvring.

However, exploiting differential drag in practice demands more than an aerodynamic model. The spacecraft must simultaneously harvest sufficient solar energy, maintain ground-station contact, and achieve high-precision payload pointing. Each function requires a specific attitude orientation, yet only one can be maintained at any time. This scheduling problem is further constrained by eclipses, narrow ground-station windows, and atmospheric density variability. Prior work has addressed these challenges largely in isolation: finite state machines (FSMs) for mode management [5], power-constrained task scheduling [6], and reinforcement-learning approaches [7].

A further challenge arises during early operations. Before ground contact can be established, the ADCS must autonomously detumble the spacecraft and achieve a stable nadir-pointing attitude. Frame-related assembly errors in the magnetometer or magnetorquer mounting must be detected and corrected onboard to prevent the controller from injecting energy. Operational experience has shown that this autonomous verification is safety-critical for CubeSats sharing a common deployer [8]. Currently, little documentation exists on the integration of these three central elements: automatic ADCS hardware verification without radio ground contact, power-constrained differential control strategies, and validation in a high-fidelity simulation environment.

This paper addresses these gaps with three contributions. First, we present a deterministic FSM governing transitions between eight ADCS modes, encoding the priority hierarchy between energy harvesting, payload pointing, ground communication, and differential drag via explicit rules and power-budget guards. Second, we describe an autonomous commissioning sequence (C1–C5) that verifies hardware frame consistency, establishes ground communication, and characterises the differential ballistic coefficient. Third, we present a stepwise differential drag control strategy managing inter-satellite separation through altitude-dependent mode assign-

This work is funded by the UK Space Agency under the ALIGN mission programme.

ment. The approach is validated using the Autonomous Laser-based Intersatellite Gigabit Network (ALIGN) mission parameters, targeting free-space optical links at 100–1000 km separation [9], [10], through a short and long-term simulation in the Basilisk astrodynamics framework [11].

The remainder of this paper describes the mission context (Sec. II), ADCS operational modes (Sec. III), and commissioning logic (Sec. IV). Sections V and VI present the FSM architecture and differential drag strategy, respectively. Finally, the simulation framework and results are discussed in Sections VII and VIII, concluding with future work in Section IX.

II. Mission Context and Concept of Operations

To define the context of the operating states, the ALGIN mission and the requirements for automatic initial pointing and the differential drag control strategy are used as examples.

A. Example Case: The ALIGN Mission

The framework is validated using the ALIGN mission parameters. ALIGN comprises two identical 6U CubeSats deployed into a sun-synchronous orbit. Each spacecraft carries the FOCUS free-space optical terminal as its primary payload and an S-band transceiver for telemetry, tracking, and commanding (TT&C). The bus, built around an Endurosat platform, features body-mounted solar panels on the $\pm Y$ and $+Z$ faces generating $\approx$77.52 W at normal incidence (4 faces with 19.38 W), a 42 Wh lithium-ion battery, and a total idle power consumption of approximately 7.4 W. The ADCS employs reaction wheels for three-axis control with magnetorquers for momentum desaturation; attitude determination combines star trackers, sun sensors, and a three-axis magnetometer [9].

B. Concept of Operations

The mission is structured into five sequential phases (Fig. 1).

1. Launch and Early Orbit Phase (LEOP). Following launch, both satellites enter a radio-silence period of 30 minutes. Upon expiration of the deployment timer, each satellite autonomously initiates the commissioning milestone C1 (sensor and actuator frame verification), which is executed during this phase. After C1 is completed, detumbling begins, reducing the angular velocity to below 1.0 deg/s. Once stabilized, each satellite orients itself towards nadir (minimum drag face), enabling initial contact with Earth.

2. Ground Communication Phase (GCP). Milestone C2 validates the full ADCS chain and ground-station link through a progressive pass-by-pass sequence. The satellites cycle between ground-station tracking, sun pointing for power recovery, and nadir as the default. Milestones C3 and C4 validate the S-band ISL and optical payload, respectively.

3. Space Communication Phase (SCP). In this phase, the health conditions of the S-band antenna for ISL and the optical communication system are tested. Each has its own commissioning procedure, C3 and C4, respectively. These are not the focus of this work, but a brief description of the test is presented.

4. Differential Drag Control Phase (DDCP). After receiving the command from ground control, flight formation control begins. The C5 milestone characterizes the differential ballistic coefficient through a brief open-loop aerodynamic drag test. The mission then enters its nominal phase, where both satellites orient themselves in Minimum Drag mode.

5. Mission. After the complete system calibration and verification of the health of each component are finished, operation begins in mission mode. In this mode, the optical intersatellite link (OISL) communication system defines the ADCS operating modes and test ranges.

Throughout all phases, a power-budget guard ensures that if the battery state of charge drops below a configurable threshold, the FSM forces a transition to sun pointing regardless of the current mode, resuming only after sufficient charge recovery. A summary of these concepts is shown in Figure 1.

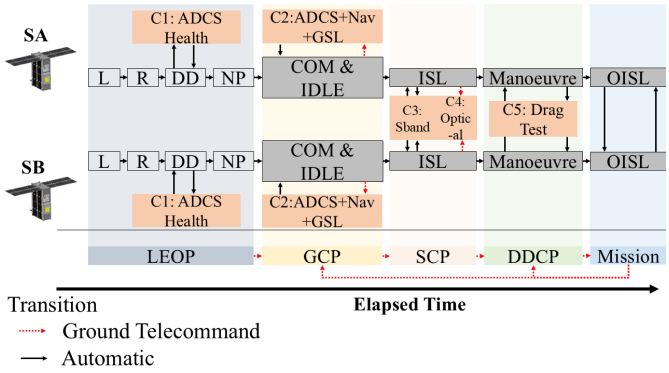

Fig. 1: Concept of operations. L: Launch, RS: Radio Silence, DD: Deployment & Detumbling, NP: Nadir Pointing. Solid arrows: automatic transitions; dashed arrows: ground telecommand. Milestones C1–C5 gate phase transitions. Safe mode is accessible from any state.

III. ADCS Operational Modes

The framework employs seven ADCS operational modes, each defining a body-frame reference orientation $[BN]$ expressed as a direction cosine matrix (DCM) whose rows are the unit vectors $\hat{\boldsymbol{r}}_1$, $\hat{\boldsymbol{r}}_2$, $\hat{\boldsymbol{r}}_3$ aligned with the body axes $+X_{\mathcal{B}}$, $+Y_{\mathcal{B}}$, $+Z_{\mathcal{B}}$ respectively.

Throughout this section: $\boldsymbol{r}$ and $\boldsymbol{v}$ denote the spacecraft inertial position and velocity, $\hat{\boldsymbol{h}} = (\boldsymbol{r} \times \boldsymbol{v})/\|\boldsymbol{r} \times \boldsymbol{v}\|$ is the orbit-normal unit vector, $n = \sqrt{\mu/r^3}$ is the mean motion, and $\boldsymbol{r}_{\mathrm{t}}$ is the target position (partner satellite or ground station). The relative position vector is $\boldsymbol{d} = \boldsymbol{r}_{\mathrm{t}} - \boldsymbol{r}$, and it is necessary to define the control decision. The details of each mode are described below.

A. Idle and Detumbling

In both modes, the reference attitude is an inertial hold $\boldsymbol{\omega}_{B/N} = \mathbf{0}$. No pointing constraint is imposed. The detumbling controller alternates between two phases. The *active* phase

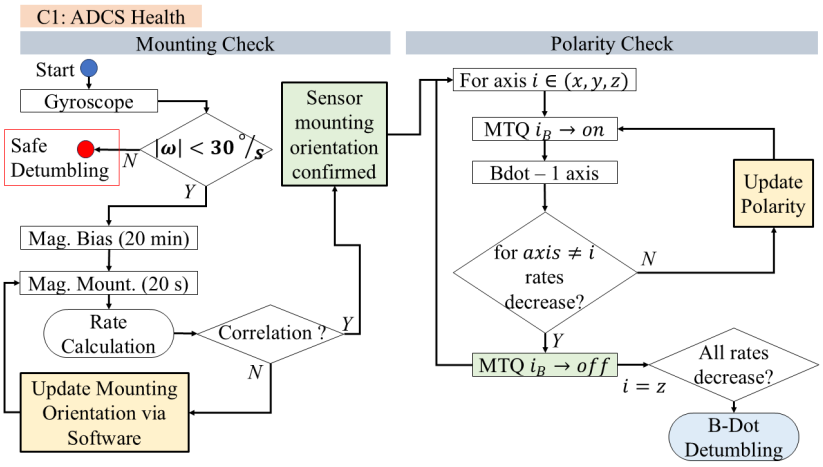

Fig. 2: C1 commissioning logic: bias estimation, frame verification via Transport Theorem residual, per-axis magnetorquer polarity test, and B-dot detumbling.

applies the well-known B-Dot control to damp all axes simultaneously. If convergence stalls, it transitions to a *despin* phase that isolates the dominant spin axis $j = \arg\max_i |\omega_i|$ via the pseudo-inverse projection

$$\mathbf{m}_{\mathcal{B}} = -\frac{k\,\omega_j}{\|\mathbf{B}_{\mathcal{B}}\|^2}\,(\mathbf{B}_{\mathcal{B}} \times \hat{\mathbf{e}}_j) \tag{1}$$

producing a pure single-axis damping torque $T_j = -k\,\omega_j\,\|B_{\mathcal{B}\perp j}\|^2$ that avoids cross-coupling. Here $\mathbf{B}_{\mathcal{B}}$ is the Earth's magnetic field in body frame.

B. Ground Link

Ground-link pointing directs $+Z_{\mathcal{B}}$ toward the ground station. The station position $\boldsymbol{r}_{\text{gs}}$ is transformed from ECEF to ECI using GMST.

C. Minimum Drag

Minimum-drag orientation aligns the long axis $(+X_{\mathcal{B}})$ with the velocity direction, presenting the smallest cross-section. A sign selection ensures the boresight faces the partner automatically:

$$s = \begin{cases} +1 & \text{if } \hat{\boldsymbol{d}} \cdot \hat{\boldsymbol{v}} > 0 \\ -1 & \text{otherwise} \end{cases} \tag{2}$$

where $\hat{\boldsymbol{d}} = \boldsymbol{d}/\|\boldsymbol{d}\|$ and $\hat{\boldsymbol{v}} = \boldsymbol{v}/v$. The reference triad is:

$$\hat{\boldsymbol{r}}_1 = s\,\hat{\boldsymbol{v}}; \quad \hat{\boldsymbol{r}}_3' = \hat{\boldsymbol{r}}_1 \times \hat{\boldsymbol{h}} \tag{3}$$

$$\hat{\boldsymbol{r}}_3 = \begin{cases} +\hat{\boldsymbol{r}}_3'/\|\hat{\boldsymbol{r}}_3'\| & \text{if } \hat{\boldsymbol{r}}_3' \cdot \boldsymbol{r} < 0 \\ -\hat{\boldsymbol{r}}_3'/\|\hat{\boldsymbol{r}}_3'\| & \text{otherwise} \end{cases} \tag{4}$$

$$\hat{\boldsymbol{r}}_2 = \hat{\boldsymbol{r}}_3 \times \hat{\boldsymbol{r}}_1 \tag{5}$$

D. Maximum Drag

Maximum-drag orientation aligns the wide face $(+Y_{\mathcal{B}})$ with velocity. The sign selection s follows the equation (2):

$$\hat{\boldsymbol{r}}_2 = s\,\hat{\boldsymbol{v}}; \quad \hat{\boldsymbol{r}}_3' = \hat{\boldsymbol{r}}_2 \times \hat{\boldsymbol{h}} \tag{6}$$

$$\hat{\boldsymbol{r}}_3 = \begin{cases} +\hat{\boldsymbol{r}}_3'/\|\hat{\boldsymbol{r}}_3'\| & \text{if } \hat{\boldsymbol{r}}_3' \cdot \boldsymbol{r} < 0 \\ -\hat{\boldsymbol{r}}_3'/\|\hat{\boldsymbol{r}}_3'\| & \text{otherwise} \end{cases} \tag{7}$$

$$\hat{\boldsymbol{r}}_1 = \hat{\boldsymbol{r}}_2 \times \hat{\boldsymbol{r}}_3 \tag{8}$$

Both drag modes share the Earth-pointing $+Z_{\mathcal{B}}$ constraint and sign-selection logic.

IV. Autonomous Commissioning Logic

The commissioning sequence (C1-C5) is designed to perform critical safety checks, with each milestone marking the transition to the next mission phase. Some of these phases (C1, C3, and C5) must operate autonomously due to communication constraints.

A. C1: Sensor and Actuator Frame Verification

C1 verifies ADCS hardware geometry autonomously before closed-loop control is permitted. An undetected magnetometer axis swap or sign flip causes the detumbling controller to inject energy, potentially rendering the spacecraft unrecoverable. A summary is present in Figure 2.

1) Hard-Iron Bias Estimation: To estimate the hard-iron bias and scale-factor/misalignment errors without prior attitude knowledge, the FSM employs an attitude-independent calibration method. By comparing the squared norm of the measured magnetic field against the onboard World Magnetic Model (WMM) reference, the attitude dependence is mathematically eliminated. The resulting linear system is solved via ordinary least squares to recover the distortion matrix and bias vector, following the standard estimation approach detailed by Markley and Crassidis [12].

Data acquisition for **20 minutes**.

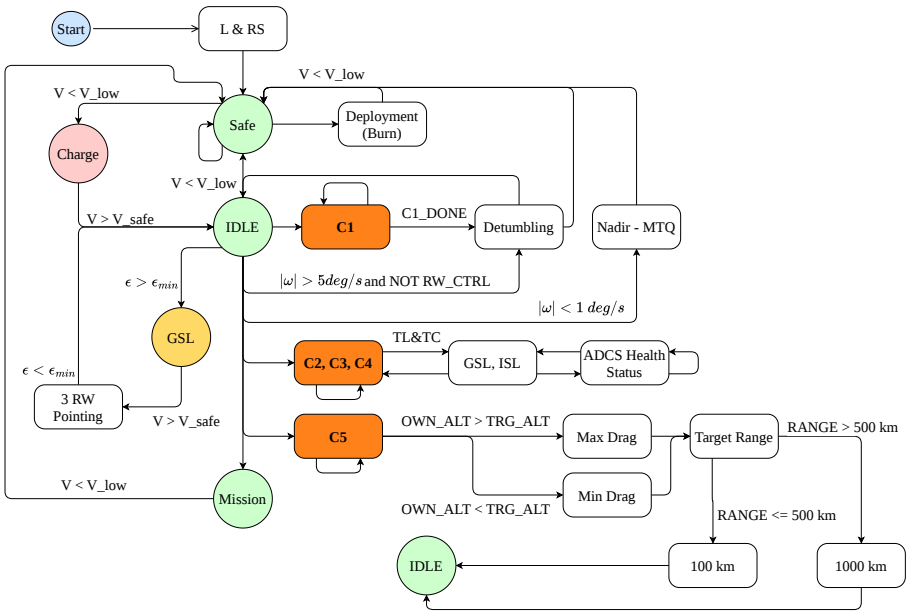

Fig. 3: Finite State Machine (FSM) architecture governing the ADCS operational modes. The logic enforces autonomous progression through commissioning milestones (C1–C5), altitude-dependent differential drag assignments, and strict power-budget guard conditions (V_{low}) that safely pre-empt nominal operations during low-power events.

2) Magnetometer Frame Verification: Assembly errors in CubeSat magnetometers arise from discrete mechanical causes (reversed flex cables, 90° PCB increments, miswired channels, failed deployment), corresponding to one of $3! \times 2^3 = 48$ signed axis permutations. After bias removal, each candidate permutation R_c is evaluated against the Transport Theorem constraint $\dot{\mathbf{B}}_{\mathcal{B}} = -\boldsymbol{\omega}_{B/N} \times \mathbf{B}_{\mathcal{B}}$ via the residual

$$J_c = \frac{1}{N} \sum_{i=1}^{N} \left\| R_c \, \dot{\mathbf{B}}_{m,i} + \boldsymbol{\omega}_{B/N,i} \times R_c \, \mathbf{B}_{m,i} \right\|^2 \tag{9}$$

The confidence metric $\eta = J_{2\text{nd}}/J_{\text{best}}$ must exceed 3.0 for the identification to be adopted.

Data acquisition for **20 seconds**.

3) Magnetorquer Polarity Verification: With the magnetometer frame resolved, a single-axis B-dot pulse is commanded on each magnetorquer independently. Cross-axis angular velocity RMS is compared against a quiescent baseline: a decrease confirms correct polarity, an increase triggers a sign flip for that axis in all subsequent operations.

Data acquisition for **60 minutes** for each axis.

B. C2–C4: Ground Link, ISL, and Optical Payload

C2 establishes the first ground-station link through a progressive four-pass sequence: connectivity test (Pass 1), bus telemetry and C1 result downlink (Pass 2), full sensor/actuator validation (Pass 3), and autonomous ground-station tracking (Pass 4). No subsequent phase transition is permitted until ground confirmation of all C2 criteria. C3 validates the S-band inter-satellite link through an autonomous ping-and-data-exchange sequence [9]. C4 calibrates the optical terminal's fast-steering mirror and laser transmitter chain [10].

C. C5: Differential Drag Characterisation

C5 constitutes the first in-orbit test of differential drag for the mission. Satellite A adopts maximum drag ($+Y_{\mathcal{B}}$ along velocity) while satellite B adopts minimum drag ($+X_{\mathcal{B}}$ along velocity, edge-on). Both maintain these attitudes for 1–2 days. The along-track separation is monitored using the TLE orbit.

The primary deliverable is the experimentally identified relative ballistic coefficient BC extracted from the measured drift rate as shown in [13]. This parameter absorbs uncertainties in individual drag coefficients, projected areas, masses, and local atmospheric density, and serves as the calibration constant for the differential drag controller in the formation control phase.

Data acquisition for **minimum 3 days for orbital parameters**.

V. Finite State Machine Architecture

The onboard mission logic is governed by a deterministic Finite State Machine (FSM) that dictates transitions between the eight ADCS operating modes. Rather than relying on ground-in-the-loop commanding for routine operations, the FSM autonomously evaluates transition conditions based on a strict priority hierarchy and power-budget guards. This ensures the spacecraft safely navigates from deployment, through the commissioning milestones (detailed in Section IV), and into nominal formation control.

A. Priority Hierarchy and Interrupt Logic

The FSM enforces a strict mode priority to continuously balance platform safety with mission objectives:

- **Power Recovery (Highest Priority):** The FSM continuously monitors the bus voltage to ensure platform safety.

If the battery depletes below a critical threshold ($V_{low} \leq 15.3$ V, corresponding to approximately 20% operational capacity), the FSM forces an immediate transition to the *Safe/Charge* state, pre-empting all other modes. The system remains in this sun-pointing recovery state until the battery reaches a resume hysteresis threshold of 15.7 V (approximately 40% capacity), preventing rapid mode oscillation during eclipses.

- **Communications and Payload:** When the ground station elevation exceeds the minimum mask ($\epsilon \geq \epsilon_{min}$) or during a scheduled inter-satellite link (ISL) window, the FSM interrupts default pointing to establish *Ground Link* or *ISL Pointing*.
- **Formation Control (Default):** During the DDCP, the default modes are *Minimum Drag* or *Maximum Drag*. These are maintained continuously to generate the required along-track drift, interrupted only by the higher-priority power or communication events above.

B. Mode Sequencing and Commissioning Integration

During early operations, the FSM acts as the strict gatekeeper for the sequential commissioning phases. For example, closed-loop detumbling and nadir-pointing modes are safely locked until the FSM registers the successful completion of the autonomous C1 frame verification. Similarly, the open-loop drag test (C5) is executed as a distinct FSM state, governed by the exact same power and communication interrupts to ensure platform safety while the relative ballistic coefficient ($\Delta\beta$) is characterized.

VI. Differential Drag Control Strategy

A. Altitude and Range-Dependent Logic

The differential drag strategy is encoded directly into the FSM (Fig. 3). Following [14], the maximum differential acceleration from the two drag configurations is

$$a_{\max} = 3\, q_{\text{ref}} \left(\frac{1}{BC_{\text{max drag}}} - \frac{1}{BC_{\text{min drag}}} \right), \qquad (10)$$

where $q_{\text{ref}} = \frac{1}{2}\rho v^2$ is the mean dynamic pressure. The controller operates on the along-track state $(\Delta s, \dot{\Delta s})$ using a bang-bang strategy with a phase-plane switching curve. At each evaluation, the braking distance $d_{\text{brake}} = \dot{\Delta s}^2/(2\, a_{\max})$ determines the regime: if the remaining error exceeds $d_{\text{brake}} + \delta$, the FSM commands full differential drag; once the error falls below this threshold, the drag roles reverse to decelerate; within the tolerance $\delta = 5\,\text{km}$ with near-zero drift, both satellites hold *Minimum Drag*.

During the acceleration and braking phases, the drag assignment is altitude-dependent to ensure monotonic drift: the satellite above the target altitude adopts *Maximum Drag* ($+Y_B$ along velocity), while the lower one holds *Minimum Drag* ($+X_B$, edge-on). The initial target separation is set by the starting range after C5: 1000 km if RANGE $>$ 500 km (stepping inward in 100 km increments), or 100 km otherwise (stepping outward).

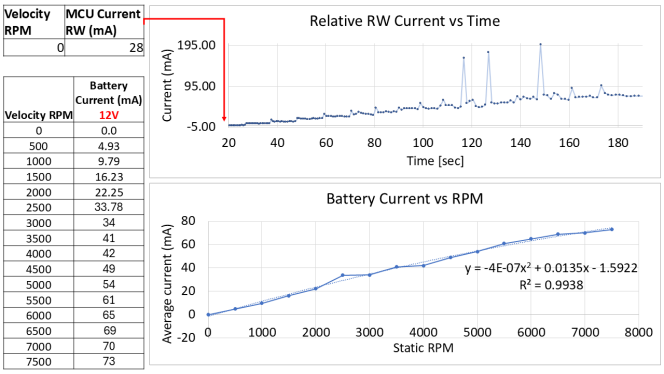

(a) RW current as a function of time and RPM. The fitted approximation is used in the simulation.

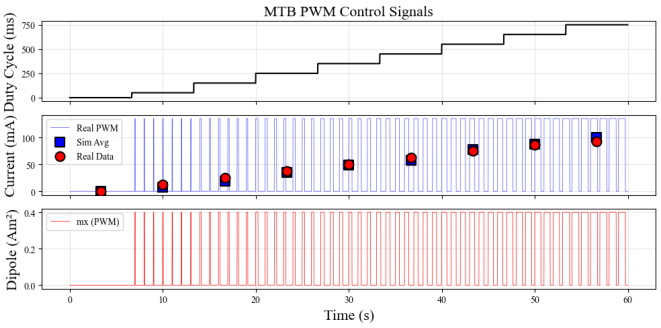

(b) MTQ magnetic moment and electrical consumption: laboratory test versus simulation model.

Fig. 4: Characterization of the actual electrical consumption of the actuators and their approximations used in the simulator.

B. Effective Duty Cycle

Under nominal conditions, continuous aerodynamic control is frequently pre-empted by the higher-priority FSM states shown in Fig. 3. Ground passes ($\epsilon > \epsilon_{min}$) force a transition to *GSL*, consuming roughly 3–5% of the orbit. Similarly, eclipse operations and power recovery ($V < V_{low}$) force transitions to *Safe/Charge*.

VII. Simulation Framework

The proposed mission logic is validated using the Basilisk astrodynamics framework [11], [15], an open-source modular simulation environment supporting multi-spacecraft dynamics with message-passing architecture.

A. Spacecraft Hardware and Power Models

The simulation incorporates flight-representative hardware models calibrated against laboratory data (Fig. 4):

- **Sensors:** 3-axis Magnetometer (1σ noise 140 nT, 50 μT hard-iron bias), Gyroscope (1σ noise 4.7×10^{-3} deg/s), and six body-mounted Coarse Sun Sensors (80° half-cone FOV).
- **Actuators:** A 3-axis magnetorquer (MTQ) assembly (0.4 Am^2 max dipole) and three body-aligned reaction wheels (RW)($J_s = 9.03 \times 10^{-6}\,\text{kg m}^2$, $\tau_{\max} = 2\,\text{mNm}$,

$\Omega_{\max} = 8000\,\text{RPM}$) with coupled jitter and friction models. Electrical consumption for both is mapped dynamically using empirical current profiles (Fig. 4).

- **Power System:** Four triple-junction GaAs solar panels (30% efficiency, 482.8 cm^2 active area per panel) with output modulated by solar incidence and eclipse shading. Energy is stored in a 42 Wh Li-ion battery, against a constant bus idle load of 7.4 W.

B. Orbital Environment

Two 6U CubeSats are propagated in a 550 km Sun-synchronous orbit ($i = 97.5°$, $e = 10^{-4}$) with J2 perturbations from the GGM03S geopotential model (degree and order 2). Atmospheric density follows the USSA76 standard atmosphere; drag forces and torques are computed per-facet using the Schaaf–Chambre free-molecular-flow model with individual specularity coefficients and wall-temperature corrections. The geomagnetic field is modelled by the WMM model, and the Sun position is obtained from SPICE ephemerides. Eclipse geometry uses cylindrical Earth-shadow entry/exit computation. Two simulation cases are considered:

1) **Commissioning (C1):** $\Delta t = 0.2$ s, 24 h duration. Open-loop dynamics with noisy sensor models; demonstrates the initial mission state including detumbling, sensor calibration, and deployable panel release. Only the chief spacecraft is fully modelled (deputy runs as a lightweight orbit-only propagator).
2) **Differential drag (C5):** $\Delta t = 0.5$ s, 3-day duration with 60 s outer-loop control steps. Both spacecraft run full ADCS with RW attitude control. The formation controller implements an altitude-dependent drag switching logic, re-evaluated every 60 s: the higher-altitude satellite is commanded to maximum-drag orientation, while the lower one holds minimum drag. Convergence is declared when the along-track separation enters a ± 5 km tolerance band around the target. The primary deliverable is the ballistic coefficient $\Delta\beta = \beta_A - \beta_B$, extracted indirectly from the secular semi-major axis decay rate via orbit-averaged sliding-window linear fits.
3) **DDCP:** Preliminary long-term demonstration of the control function of Section VI to adjust the range to the desired distance.

VIII. Results and Discussion

A. C1 Commissioning Validation

The autonomous C1 sequence is validated in the Basilisk simulation. Fig. 6 shows the magnetometer and gyroscope data over the full commissioning window. The frame verification algorithm identifies the correct mounting permutation with confidence ratio $\eta > 5$, and the subsequent polarity test confirms all three magnetorquer axes. B-dot detumbling then reduces the angular rates to below $\omega_{\text{thr}} = 0.6$ deg/s within approximately 3 orbits.

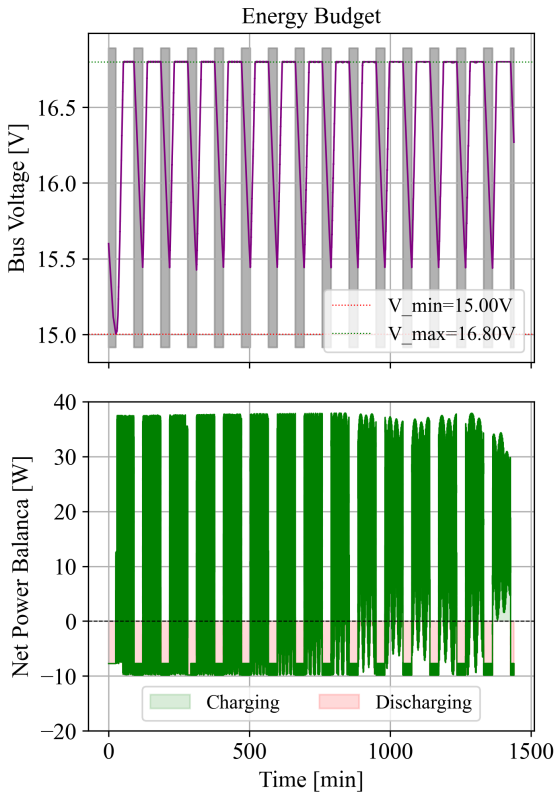

Fig. 5: Bus voltage and net power balance during the formation control phase. Positive net power indicates battery charging; negative indicates discharge. The battery remains within operational bounds throughout the simulation.

B. Power Balance and Mode Duty Cycles

Fig. 5 shows the bus voltage and net power balance during the formation control phase. The battery voltage remains within 15.0–16.8 V throughout the simulation. The mode duty cycles over the 30-day run are: Min./Max. Drag ≈85%, Sun Pointing ≈8%, Ground Link ≈4%, Nadir ≈3%. The power-budget guard is triggered an average of 1.2 times per day, with recovery to $\text{SoC}_{\text{resume}}$ typically completed within one sunlit arc.

C. C5: Drag Test

The key result of the differential drag analysis is that the 6U constellation characterized the ballistic coefficient in the early state of the mission. Fig. 7 presents the 3-day differential drag characterisation. Separation decreases from ∼1800 km toward the 1000 km target at an instantaneous rate of -82.9 km/day. While this initial rate includes local orbital and density variations, the long-term sustained drift—accounting for FSM interrupts—averages ≈400 km/month (Fig. 8). Per-orbit ballistic coefficient estimates align with expected geometric values ($BC_{\text{max drag}} = 69.9$ kg/m^2, $BC_{\text{min drag}} = 139.7$ kg/m^2). Periodic BC spikes correlate with ground-station passes (Section V), where the FSM pre-empts the drag attitude. This orientation reduces the cross-sectional area, diminishing orbit-

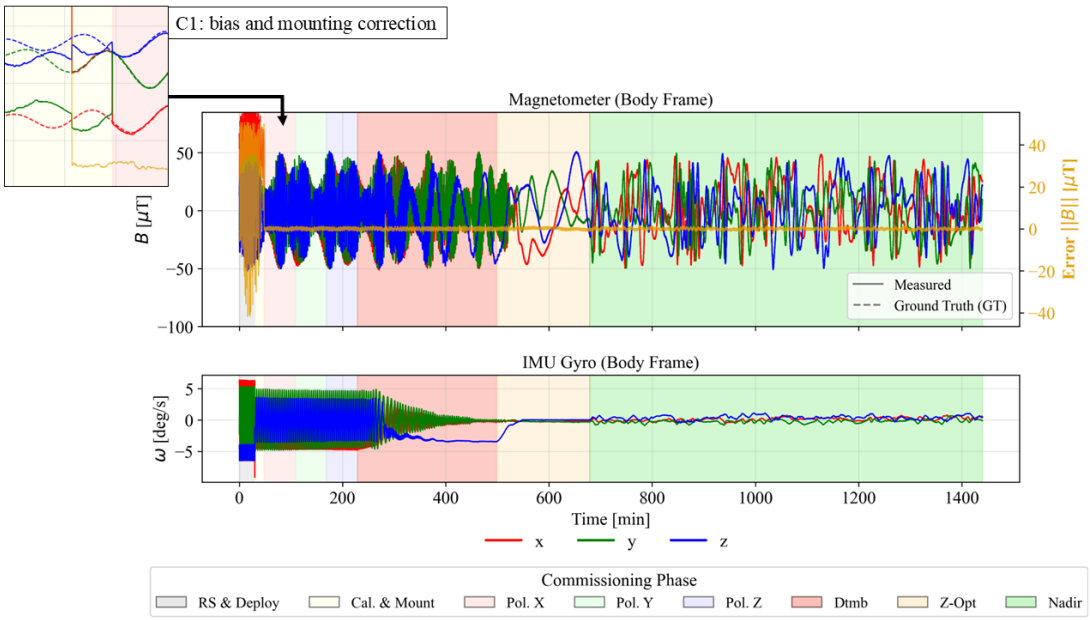

Fig. 6: Validation of the C1 commissioning sequence: magnetometer measurements (top) and gyroscope rates (bottom) over 1400 minutes. Shaded regions indicate commissioning sub-phases: radio silence and deployment (grey), frame calibration and mounting verification (green), per-axis magnetorquer polarity tests (coloured), and B-dot detumbling (red). The magnetometer error (right axis, orange) confirms convergence of the bias estimate.

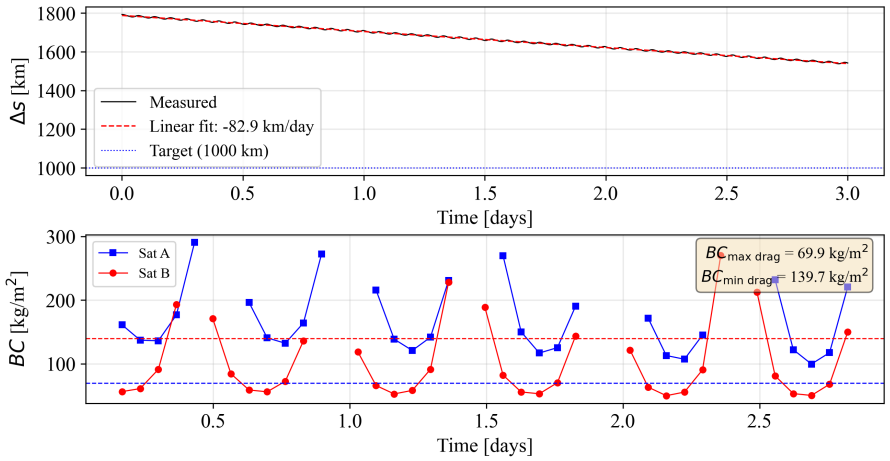

Fig. 7: C5 differential drag characterisation: along-track separation with linear fit (top) and per-orbit ballistic coefficient estimates (bottom). Dashed lines show expected geometric BC values. Excursions above nominal bounds coincide with ground-station passes, where the FSM redirects both spacecraft to ground-link attitude, presenting a different cross-section to the drag and biasing those orbit-averaged BC estimates.

averaged drag and producing transient BC estimates exceeding $BC_{\text{min drag}}$. These outliers match the expected 2–3 daily ground contacts.

While high-fidelity density models improve analytical BC estimation, persistent environmental uncertainties and non-linear interruptions from higher-priority FSM modes (e.g., communications, sun-pointing) degrade the effective drag duty cycle. Consequently, precise analytical maneuver planning becomes highly complex. Evolutionary optimization and machine learning tools offer a robust pathway to adaptively tune this control logic under non-ideal operational conditions [16], [17] .

D. DDCP: Long-term simulation test

To evaluate the impact of these non-linearities, Fig. 8 compares the baseline deterministic controller with a Genetic

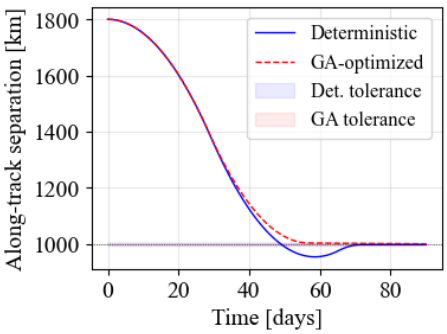

Fig. 8: Along-track separation: deterministic three-phase controller vs. GA-optimised parameters. Shaded bands denote ± 5 km tolerance.

Algorithm (GA)-optimised variant. The deterministic law [14] assigns maximum drag to the higher-altitude satellite using fixed-threshold phase-plane braking. While reliable, assuming continuous drag in a heavily scheduled FSM environment yields a conservative approach with mild overshoot.

The GA-optimised profile mitigates this by jointly tuning switching parameters over candidate trajectories, inherently accounting for degraded duty cycles and non-linearities to reduce both convergence time and overshoot. As demonstrated in [16], such evolutionary optimisation can incorporate environmental uncertainties and periodic schedules (e.g., ground-station access), accurately capturing the coupled effect of FSM interrupts on maneuver performance.

IX. Conclusions and Future Work

This paper presented a deterministic finite state machine for autonomous management of different ADCS operational modes on a twin CubeSat formation using differential drag as the sole propellantless manoeuvring mechanism. The framework integrates power-budget guard conditions, autonomous commissioning (C1–C5), and a stepwise distance control strategy. Validation using the ALIGN mission parameters in the Basilisk simulator demonstrated a relative along-track drift exceeding 400 km per month (Fig. 8) while maintaining positive energy balance, with an effective drag-mode duty cycle of approximately 85%.

The simulation also reveals that higher-priority FSM interrupts, particularly ground-station passes, introduce measurable perturbations in the per-orbit ballistic coefficient estimates, confirming that the effective duty cycle of the drag modes is a first-order consideration for formation control performance. A GA-optimised variant achieves faster convergence with reduced overshoot, suggesting that population-based methods can further exploit the available differential acceleration within the same FSM architecture.

Future work will focus on integrating learning-based algorithms to refine the ballistic coefficient estimation in orbit and to optimise the control switching parameters with the ground station access and sun-pointing schedules across the representative mission scenarios.

Acknowledgment

The authors acknowledge the UK Space Agency for funding the ALIGN mission. The ALIGN consortium comprises Northumbria University, Durham University CfAI, SMS Electronics, and Telespazio, with Lockheed Martin UK Space and Endurosat as key subcontractors.

References

[1] C. L. Leonard, W. M. Hollister, and E. V. Bergmann, "Orbital formationkeeping with differential drag," *Journal of Guidance, Control, and Dynamics*, vol. 12, no. 1, pp. 108–113, 1989.

[2] B. S. Kumar, A. Ng, K. Yoshihara, and A. de Ruiter, "Differential drag as a means of spacecraft formation control," *IEEE Transactions on Aerospace and Electronic Systems*, vol. 47, no. 2, pp. 1125–1135, 2011.

[3] C. Foster, H. Hallam, and J. Mason, "Constellation phasing with differential drag on Planet Labs satellites," *Journal of Spacecraft and Rockets*, vol. 55, no. 5, pp. 1198–1208, 2018.

[4] C. Traub, M. Ben-Larbi, F. Turco, K. Briess, and S. Fasoulas, "Operationalizing differential drag control: A planning routine for the S-NET satellite formation," *CEAS Space Journal*, 2025, published online.

[5] G. Di Mauro, M. Lawn, and R. Bevilacqua, "A low-thrust finite state machine based controller for N-satellites formations in distributed synthetic aperture radar applications," *Acta Astronautica*, vol. 203, pp. 492–510, 2023.

[6] C. A. Rigo, L. O. Seman, E. Camponogara, E. M. Filho, and E. A. Bezerra, "Task scheduling for optimal power management and quality-of-service assurance in CubeSats," *Acta Astronautica*, vol. 179, pp. 550–560, 2021.

[7] A. T. Harris and H. Schaub, "A comparative analysis of reinforcement learning algorithms for earth-observing satellite scheduling," *Frontiers in Space Technologies*, vol. 4, 2023.

[8] C. Garrido, E. Obreque, M. Vidal-Valladares, S. Gutierrez, M. D. Quezada, C. Gonzalez, C. Rojas, and T. Gutierrez, "The First Chilean Satellite Swarm: Approach and Lessons Learned." Small Satellite Conference, 2023.

[9] R. Zia-Ul-Mustafa, C. Graham, E. Obreque, R. Binns, E. Scullion, R. Wicks, J. Martin, A. Riaz, N. Khorchef, J. Vernon, and C. Bourgenot, "Pointing, acquisition, and tracking (pat) for optical satellite communications: Recent trends and the align uk mission's pat mechanism," in *2025 IEEE International Conference on Space Optical Systems and Applications (ICSOS)*, 2025, pp. 1–10.

[10] A. Riaz, E. Scullion, R. Wicks, Z. Ahmed, E. Obreque, N. Khorchef, J. Vernon, C. del Valle, R. Zia-ul Mustafa, R. Binns *et al.*, "Characterisation of amplified laser beam profiles subject to changing edfa pump currents in cubesats," in *Free-Space Laser Communications XXXVIII*, vol. 13885. SPIE, 2026, pp. 355–366.

[11] P. W. Kenneally, S. Piggott, and H. Schaub, "Basilisk: A flexible, scalable and modular astrodynamics simulation framework," *Journal of Aerospace Information Systems*, vol. 17, no. 9, pp. 496–507, 2020.

[12] F. L. Markley and J. L. Crassidis, *Fundamentals of Spacecraft Attitude Determination and Control*, ser. Space Technology Library. New York: Springer-Verlag, 2014, vol. 33.

[13] L. Cament, M. Adams, E. Obreque, and P. Barrios, "Adaptive Tracking of Space Objects using Riemannian Manifolds on the 2-Sphere," in *The Advanced Maui Optical and Space Surveillance (AMOS) Technologies Conference*, S. Ryan, Ed., Sep. 2025, p. 45.

[14] C. Foster, J. Mason, V. Vittaldev, L. Leung, V. Beukelaers, L. Stepan, and R. Zimmerman, "Constellation phasing with differential drag on Planet Labs satellites," *Journal of Spacecraft and Rockets*, vol. 55, no. 5, pp. 1198–1208, 2018.

[15] M. Vaz Carneiro and H. Schaub, "Small satellite formation flying application using the Basilisk astrodynamics software architecture," in *International Workshop on Spacecraft Formation Flying (IWSCFF)*, 2019, iWSCFF 19-88.

[16] E. Obreque and M. Díaz, "An effort to use a solid propellant engine arrangement in the moon soft landing problem," *Aerospace*, vol. 9, no. 10, p. 540, 2022.

[17] S. D. Melaku and H.-D. Kim, "Optimization of multi-mission cubesat constellations with a multi-objective genetic algorithm," *Remote Sensing*, vol. 15, no. 6, p. 1572, 2023.